DOI: 10.24352/UB.OVGU-2017-009 TECHNISCHE MECHANIK, 36, 1-2, (2016), 32 – 56
submitted: July 24, 2015

Modelling the Microstructure and the Viscoelastic Behaviour of Carbon Black Filled Rubber Materials from 3D Simulations

B. Figliuzzi, D. Jeulin, M. Faessel, F. Willot, M. Koishi, N. Kowatari

Volume fraction and spatial repartition of fillers impact the physical properties of rubber. Extended percolating networks of nano-sized fillers significantly modify the macroscopic mechanical properties of rubbers. Random models that describe the multiscale microstructure of rubber and efficient Fourier-based numerical algorithms are combined to predict the material's mechanical properties. From TEM image analysis, various types of multiscale models were proposed and validated, accounting for the non-homogeneous distribution of fillers: in the present work, aggregates are located outside of an exclusion polymer simulated by two families of random models. The first model generates the exclusion polymer by a Boolean model of spheres. In the second model, the exclusion polymer is a mosaic model built from a Johnson-Mehl tessellation. Here the exclusion polymer and the polymer containing the filler show a similar morphology, contrary to the Boolean model. Aggregates are then described as the intersection of a Boolean model of spheres and of the complementary of the exclusion polymer. Carbon black particles are simulated by a Cox model of spheres in the aggregates. The models rely on a limited number of parameters fitted from experimental covariance and cumulative granulometry. The influence of the model parameters on percolation properties of the models is studied numerically from 3D simulations. Finally, a novel Fourier-based algorithm is proposed to estimate the viscoelastic properties of linear heterogeneous media, in the harmonic regime. The method is compared to analytical results and to a different, time-discretized FFT scheme. As shown in this work, the proposed numerical method is efficient for computing the viscoelastic response of microstructures containing rubbers and fillers.

1 Introduction

Mechanical properties of rubbers are often improved by including nanoscopic fillers in their composition. Usually, silica and carbon black materials are used for this purpose. The geometrical properties of the fillers are an important feature of the global material. In particular, their volume fraction and spatial distribution largely determine the physical properties of the rubber. Extended percolating networks of fillers can for instance significantly enhance the mechanical properties of rubbers on macroscopic scales.

This work investigates the influence of the fillers geometry on the viscoelastic properties of rubber. An important step toward the completion of this research is the development of random models describing their complex microstructure. Following a now well-established method in material science as in Jeulin (1991), random realizations of these models can in turn be used to perform an extensive study of the mechanical properties of the rubber.

As reviewed by Jean et al. (2011a), several models have been developed in the past 20 years to describe the microstructure of rubbers. Bergström (1998) developed a model describing the carbon aggregates as squares or dodecahedra in an elastomeric volume. Even if their model only accounts for the scale of aggregates, they were able to conduct extensive finite elements calculations aimed at describing the large deformation behavior of the rubber. Relying on a similar approach, Jha et al. (2007) developed a cuberbille model to describe carbon aggregates in a rubber matrix. In their model, they notably added a third phase accounting for a layer of bound rubber surrounding the aggregates. Naito et al. (2007) improved the microstructure description by considering that aggregates can be represented as the union of carbon black spherical-shaped particles, eventually opening the way to the development of more accurate models. Carbon black composites have finally been widely investigated at

the Center for Mathematical Morphology by Jeulin and Le Cöent (1996), Savary et al. (1999), Delarue and Jeulin (2003) and Moreaud and Jeulin (2005).

In this paper, we first introduce the studied material nanostructure from TEM micrographs. After a morphological segmentation of images, measurements are performed to quantitatively characterize the microstructure. Then, two random set models to reproduce the multiscale microstructure of rubbers are developed. They are identified from the available experimental data obtained on TEM images and on simulations. In Section 4, we focus on the issue of percolation, which is of particular interest regarding the microstructure optimization. In the last part, viscoelastic properties of the material are predicted by means of Fast Fourier Transforms performed on simulated 3D images generated from the random model.

2 TEM Images Analysis

2.1 Material

This work concerns a rubber material reinforced by carbon black particles as fillers, that are embedded in a matrix of rubber and can be geometrically well-approximated by spheres of diameter $D \simeq 30 - 40$ nm, as illustrated in Figure1 a. The volume fraction of the fillers is around 14 percents in the rubber. A key feature of the material is that the rubber matrix is constituted of two distinct polymers: an exclusion polymer, which cannot contain any filler, and its complementary polymer, which can contain fillers. Fillers tend to agglomerate together within the rubber matrix. The filler particles indeed exhibit a turbostratic structure which enable them to merge and create aggregates (Jean et al. (2011a)).

2.2 TEM images Segmentation

To analyze the rubbers microstructure, we dispose of a set of 50 TEM micrographs of size 1024 by 1024 pixels with resolution 2.13 nm per pixel. These images were obtained in the *Yokohama Rubber Research Center*. The slices of material probed by the microscope have a thickness around 40 nm. The first task is to segment these images, in order to identify the spatial distribution of the fillers. The segmentation procedure and its results are presented in the first two paragraphs of this section. The next step is to extract morphological characteristics from the segmented TEM images, as described in the third paragraph.

Algorithm The segmentation process aims at extracting the carbon black phase from the 8 bits TEM images. White regions can be observed in the images, which correspond to aggregates prints that have been taken off by the blade of the microtome during the samples preparation. These prints have to be included in the set of regions to be extracted. The main difficulty here is the presence of an illumination gradient and of contrast difference. Therefore, a simple thresholding is not sufficient to discriminate the black visible aggregates from the rubber matrix.

The first step of the segmentation consists in denoising the TEM images. The denoising is performed using an alternate sequential filter, a classical filter in mathematical morphology (Serra (1982)).

The second step of the segmentation process is the extraction of the white aggregates prints. This task is easily performed by thresholding the filtered image with a grey level higher than 170. Finally, the prints with area smaller than 3 pixels are removed from the thresholded image.

The third step of the segmentation process is the extraction of the visible black carbon aggregates. First, the white prints of aggregates are extracted by an opening with a disc of radius 50 pixels to the filtered image, followed by a geodesic reconstruction. Once the white prints have been removed, a black top hat is performed, to account for contrast difference in the image and to detect the darkest zones. A closing of size 20 pixels is used in this purpose. The top hat introduced by Meyer (1979) is a morphological operator which returns the difference between an original image and that same image after opening by some structuring element. This operator is classically used to remove the large scale contrast in an image. A black top hat is simply a top hat operator applied on the inverse image. At this point, a threshold on the resulting image extracts the visible black aggregates, with a grey level around 15. This threshold level is specified to recover an average apparent area fraction of fillers close to 28

percents for the available TEM images. This apparent area fraction results from the projection of the particles on the image during the acquisition by TEM on slices with a thickness approximately twice the radius of a black carbon particle. Finally, the aggregates with area lower than 3 pixels are removed by an area opening applied to the thresholded image.

The results of the segmentation procedure are shown step by step for an initial TEM image in Figure 1.

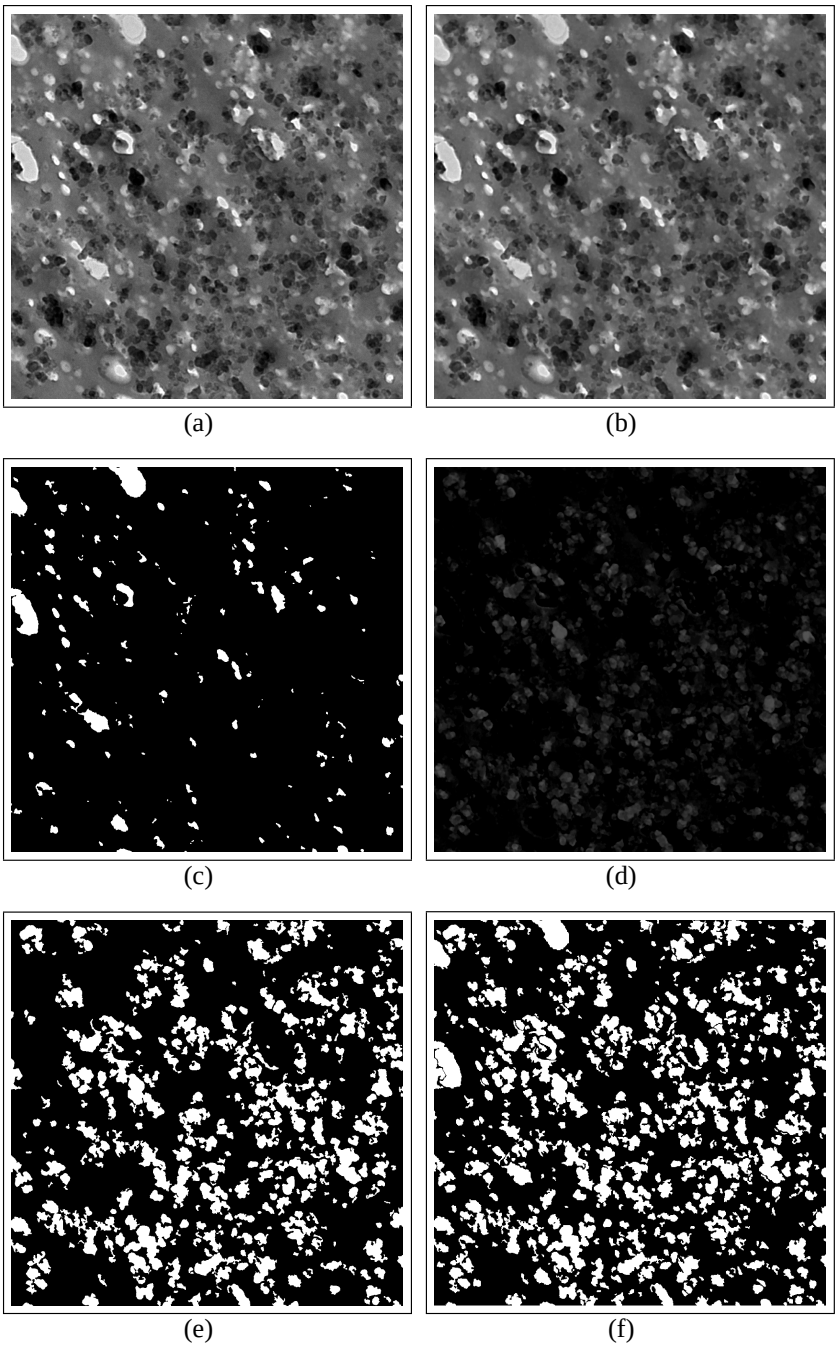

Figure 1: (a) TEM Image of rubber matrices filled with carbon black, obtained in the Yokohama Rubber Research Center. Different steps of the segmentation (see text): (b) Filtered TEM Image; (c) Extracted white prints; (d) Dual Top-hat; (e) extracted aggregates; (f) segmented image.

Morphological analysis An efficient way to keep track of the information embedded in the segmented images is to rely on a morphological characterization of the material. In this work, use is made of the covariance, to measure scales in the images, and of size distributions of the filler by opening transformations.

The covariance of a random set A is the probability that x and $x + h$ both belong to A:

$$C(x, x + h) = P\{x \in A, x + h \in A\}, \tag{1}$$

where h is some vector of $\mathbb{R}^n$. For a stationary random set, the covariance is a function of the distance h only:

$$C(x, x + h) = C(h). \tag{2}$$

The covariance $C(h)$ provides useful information about the spatial arrangement of the random set A and can account for the presence of several scales in the studied set or for periodicity. By definition, $C(0)$ simply corresponds to the volume fraction p of the set A. In addition, the covariance $C(h)$ reaches a sill at the distance or range d. At this distance, we have

$$C_A(d) = p^2. \tag{3}$$

The average covariance measured on segmented binary images is given in Figure 2.

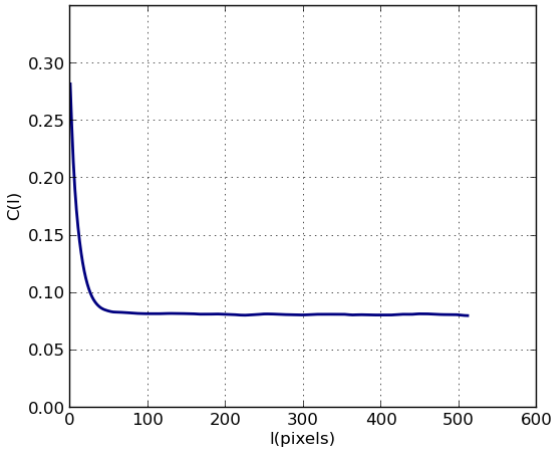

Figure 2: Experimental covariance measured on segmented images

Another important statistical characteristic is the granulometry of the material. The axiomatic of granulometries was first formulated in Matheron (1975). In this work, we will consider a granulometry relying on a family of openings by disks. Let K be a convex set. We consider the family $\{K_\lambda, \lambda > 0\}$, where $K_\lambda = \lambda K$. The opening operator (the symbols $\ominus$ and $\oplus$ representing the morphological erosion and dilation)

$$\Phi_\lambda(A) = (A \ominus \check{K_\lambda}) \oplus K_\lambda, \tag{4}$$

defined for all closed set A, is a granulometry. Therefore, the granulometry by openings provides a convenient way to characterize the size distribution of the aggregates in the material. The cumulative granulometry curve of the carbon black filler, deduced from the changes of volume fraction measurement with the size λ, is shown in Figure 3.

Using the covariance and the granulometry curves, we can select a proper set of parameters for the identification of random sets models and control their validity, as explained in the next section.

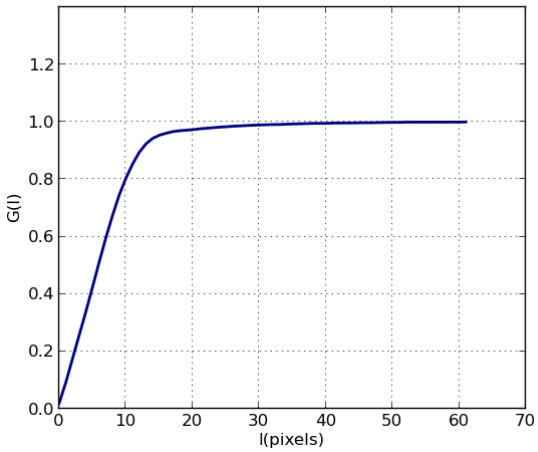

Figure 3: Experimental cumulative size distribution of the carbon black filler obtained by openings by discs.

3 Random Models of Multiscale Microstructures

As suggested by the intrinsic nature of the material and as observed after the segmentation, the fillers tend to regroup in the material to create aggregates. As a consequence, we have to rely on a two-scale model to properly describe the microstructure (Jeulin (2010, 2012)). The first scale corresponds to the aggregates, while the second one describes more specifically the single particles inside the aggregates.

In addition, several alternatives can be considered to locate the aggregates outside of the exclusion polymer. scale. In this work, two distinct models are used in this purpose. The first one relies on a Boolean model of spheres of constant radius to model the exclusion polymer distribution, the second one on Johnson-Mehl tesselations. In both cases, the location of the centers of carbon black spheres are located according to a Poisson point process restricted to the permitted zones, namely outside of the exclusion polymer and inside the aggregates, generating a Cox Boolean model of spheres (Jeulin (2010, 2012)). Both models are presented and discussed in this section. All simulations presented here are realized using the software VtkSim, developed in Faessel (2012); Faessel and Jeulin (2011) at the Center for Mathematical Morphology. The method used for the implementation is briefly introduced later in this section.

3.1 Exclusion Polymer based on a Boolean Model of Spheres

3.1.1 Theoretical Model

The first model relies on the Boolean model (Matheron (1975)). As eluded to earlier, the studied material contains two kinds of polymers:

- an exclusion polymer $\mathcal{P}_e$ with volume fraction v_e
- a second polymer $\mathcal{P}_i$ with volume fraction v_i that can contain fillers.

The exclusion polymer is modelled by a Boolean model of spheres of constant radius R_e (Figure 4 a) The model depends on two parameters: the intensity θ_e of the underlying Poisson point process and the exclusion radius R_e. These two parameters can be related to the volume fraction of exclusion polymer to yield

$$1 - v_e = \exp(-\theta_e \frac{4\pi}{3} R_e^3). \tag{5}$$

Therefore, if the volume fraction of the exclusion polymer is known, the exclusion polymer modelling is controlled by one single parameter. The second polymer is obtained as the complementary of the exclusion polymer. At this

point, the spatial distribution of aggregates still has to be simulated. Aggregates are modelled as the intersection of the polymer $\mathcal{P}_i$ and of a Boolean model of spheres with radius R_a, independent from the model used to simulate the exclusion polymer (Figure 4 b). Again, the model is described by two parameters: the intensity θ_i of the underlying Poisson point process, and the radius R_i of the implanted spheres. The volume fraction v_a of the aggregates is given by

$$v_a = (1 - v_e)\left(1 - \exp(-\theta_i \frac{4\pi}{3} R_i^3)\right). \tag{6}$$

The second scale of the material is made of the carbon black particles themselves. These particles are simulated using a Boolean model of spheres of constant radius R_{cb} implanted on the realization of a Cox point process driven by the aggregates. Since the carbon black particles exhibit a turbostratic structure, these particles can interpenetrate. Therefore, in the model, the particles can partially overlap by introduction of a hard-core distance equal to the radius of the particle (Figure 4c).

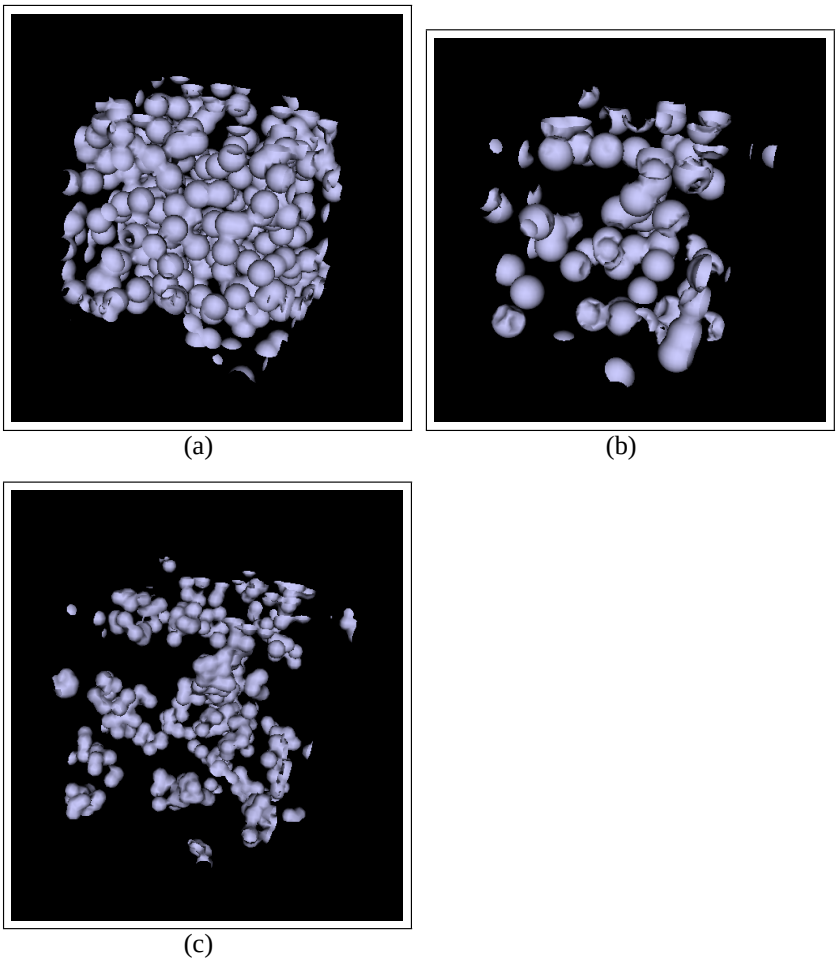

Figure 4: The three steps of the construction of the model: (a) exclusion polymer (Boolean model of spheres); (b) aggregates; (c) carbon black particles network ($v_e = 0.2$; $R_e = 30$ nm; $R_a = 60$ nm; $R_{cb} = 20$ nm; simulated volume: (500 nm)^3)

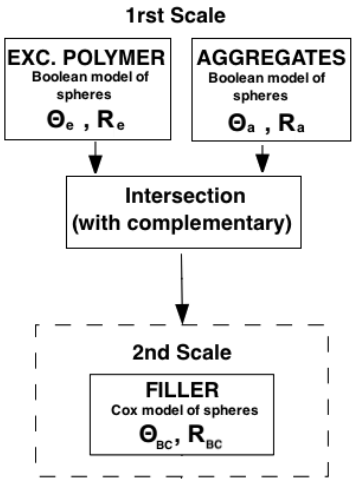

Figure 5: Scheme of the multiscale random model (exclusion zones made of a Boolean model of spheres)

The intensity of this Cox process is the random measure defined by

$$\theta_{cb}(x) = \begin{cases} \theta & \text{if } x \in A_{aggr} \\ 0 & \text{otherwise} \end{cases} \tag{7}$$

The overall construction of the model is summarized in Figure 5. A vectorial simulation of a domain with a $1\mu m^3$ volume is generated in 2 minutes.

Concerning the parameters of the model, the radius of the spheres can be measured experimentally. Therefore, the modelling of the second scale is entirely controlled by the single parameter θ_{cb}. Overall, if the volume fraction v_e of exclusion polymer and if the radius R_{cb} of the carbon black particles are known, the global model is controlled by the following set of parameters:

- the intensity θ_e of the Poisson point process aimed at describing the exclusion polymer,
- the intensity θ_a of the Poisson point process on which the modelling of the aggregates relies,
- the radius R_a of the Boolean spheres used to model the aggregates,
- the intensity θ_{cb} of the Cox point process on which relies the modelling of the spatial distribution of the black carbon particles.
- the hard-core distance for the Cox point process, which is equal to the radius of the particle.

Finally, note that a bound rubber of constant thickness t surrounds the carbon black particles. In the model, the bound rubber is obtained by considering the Boolean difference of a boolean model of sphere of constant radius $R_{cb} + t$ implanted on the centers of the black carbon particles and of the Boolean spheres describing the black carbon particles.

This version of the model is close to the version given in (Jean et al. (2011a)). However in the previous work, aggregates were obtained from a Boolean model of spheroids, instead of spheres, and no hard-core process was introduced for the location of carbon black particles. Furthermore, the identification process of the parameters of the model was completely different.

3.1.2 Model Fitting from Experimental Data

The model can be identified and validated with the available experimental data. The four free parameters R_e, R_a, θ_a and R_{cb} are estimated by fitting the covariance and the granulometry curves of the simulated images to the corresponding experimental curves.

Optimization algorithm The procedure to fit the model parameters is as follows. First, we start from the experimental covariance $\tilde{C}(h)$ for all distances $0 \leq h \leq N$ and the experimental granulometry curve $\tilde{G}(s)$ for all sizes $1 \leq s \leq K$. Then, for each realization of the model the least square function is computed

$$\mathcal{F}(R_e, \theta_a, R_a) = \sum_{n=0}^{N} (C[R_e, \theta_a, R_a, n] - \tilde{C}[n])^2 + \sum_{k=1}^{K} (G[R_e, \theta_a, R_a, k] - \tilde{G}[k])^2, \tag{8}$$

where C (resp. G) is the covariance function (resp. granulometry curve) measured at all distances $\{0 \leq n \leq N\}$ (resp. for all sizes $\{0 \leq k \leq K\}$) on the realization. The optimization problem is thus the determination of the parameters that minimize the functional $\mathcal{F}$.

Considering the lack of analytical formulae for the covariance in the model, we have to rely on numerical procedures to perform the optimization. Most numerical optimization algorithms rely on steepest-descent or on Gauss procedures. A popular method in numerical optimization is thus the Levenberg-Marcquardt algorithm (Levenberg (1944)), which combines these two approaches. This algorithm has been successfully used in (Jean et al. (2011a)) to optimize a similar model for the microstructure of carbon black particles embedded in rubbers. The main issue with the Levenberg-Marcquardt algorithm is that it relies on a gradient calculation. Estimating the gradient of the covariance with respect to the simulation parameters is a difficult task here, since a small variability cannot be avoided due to the intrinsic probabilistic nature of the model. As a consequence, in the present work another classical optimization algorithm is implemented to perform the optimization, namely the Nelder-Mead procedure (Nelder and Mead (1965)) . The advantage of this algorithm is that it does not rely on the gradients of the functional with respect to the parameters.

Results and discussion The values of the parameters obtained after optimization are given in the Table 1. Note that a particular emphasis was given to the covariance fitting, as evidenced in Figure 6. A simulated image is shown in Figure 7 and compared to a segmented TEM image.

It is clear from Figure 6 that the model accurately reproduces the reference covariance curve for the studied material. However, a small but still significant discrepancy can be observed between the reference granulometry and the simulations. This is a direct consequence of the model chosen to describe the microstructure. By using a Boolean model to describe the exclusion polymer, strict limitations are imposed on the aggregates geometry. In addition, the model does not preserve the geometrical symmetry between the exclusion polymer and its complementary. As a consequence, the model fails to properly simulate the smallest aggregates, which explains the discrepancy between the granulometry curves. This discrepancy can also result from the aggregate prints removed during the sample preparation: they were considered to be originally mostly constituted of black carbon particles, but this remains an approximation. Hence, the granulometry of the larger grains is largely overestimated, which strongly impacts the granulometry features.

It is finally interesting to take a closer look at the optimal parameters, and in particular at the intensity of the Cox model for the carbon black particles. One can note that the intensity of the Cox model yields a significantly high value. This is explained by the high density of carbon black particles in the aggregates.

v_e	R_e (nm)	θ_a (nm^{-3})	R_a (nm)	θ_{cb} (nm^{-3})	R_{cb} (nm)
0.2	30	4.0×10^{-7}	60	3.0×10^{-5}	18

Table 1: Optimized parameters for the Boolean model of exclusion polymer

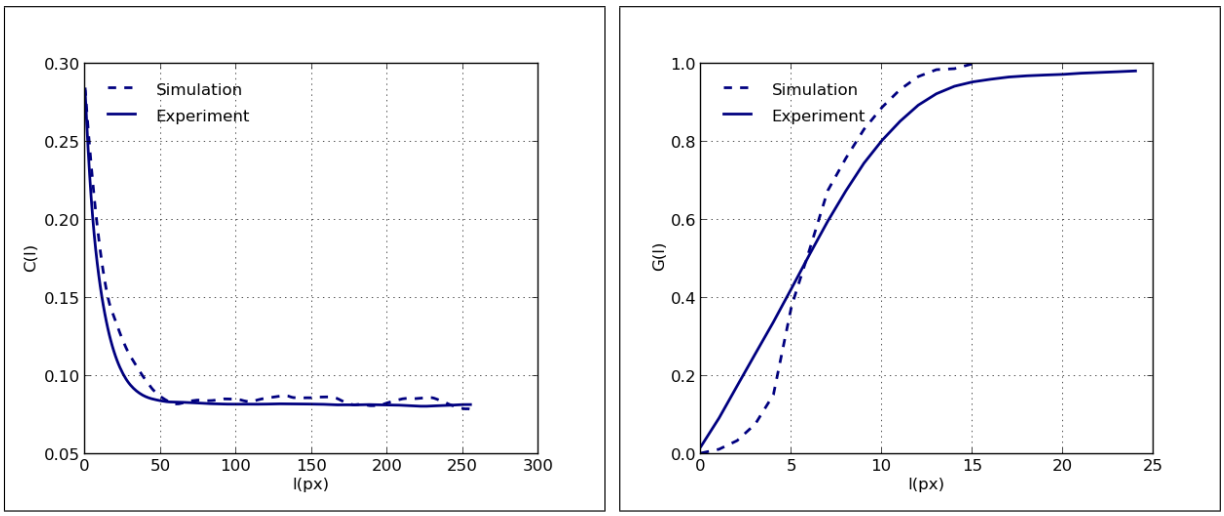

(a) (b)

Figure 6: Covariance (a) and granulometry (b) of the simulated material. The simulated curves are represented by the discontinuous lines, the experimental curves by the continuous lines.

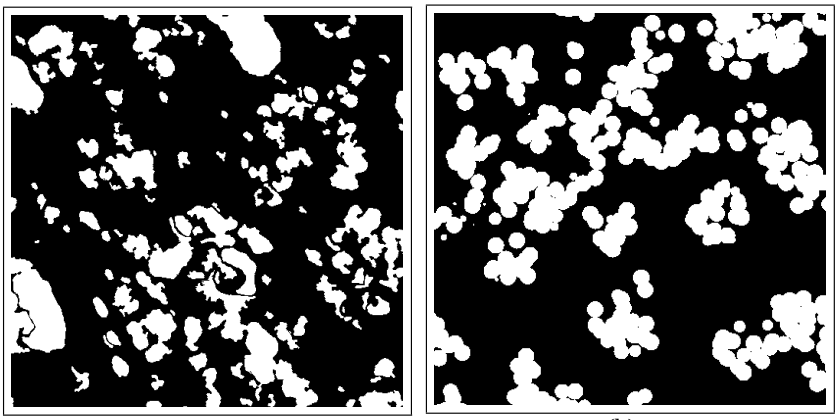

(a) (b)

Figure 7: Comparison between an experimental (a) and a simulated TEM image (b) for the Boolean model of exclusion polymer.

3.2 Exclusion Polymer based on a Johnson-Mehl Mosaic Model

As indicated previously, a major issue regarding the Boolean model is that it does not preserve the geometrical symmetry between the exclusion polymer and its complementary. It is therefore of interest to consider other models to describe the exclusion polymer. For this purpose, a model for the exclusion polymer based upon Johnson-Mehl tesselations is introduced in this section.

3.2.1 Theory

Let Ω denote a given volume in $\mathbb{R}^3$. A tessellation in Ω is a subdivision of Ω into three dimensional subsets referred to as *cells*. A general theory of random tessellation has been established over the years, notably by Matheron (1969)), Stoyan et al. (1995), Zähle (1988) and Møller (1989). Another useful reference on this topic is the book of Schneider and Weil (2008). Finally, note that the paper of Møller (1992) provides a unified exposition of random Johnson-Mehl tessellations

The Johnson-Mehl tessellation model was introduced by Johnson and Mehl, mainly to describe crystallization pro-

cesses in metallography. Their model can be seen as a variation of the Voronoï model. A Voronoï tessellation is a tessellation built from a Poisson point process $\mathcal{P}$ in the space $\mathbb{R}^3$. Every point x of $\mathbb{R}^3$ is associated to the class $\mathcal{C}_i$ containing all points of $\mathbb{R}^3$ closer from the point x_i of $\mathcal{P}$ than from any other point of $\mathcal{P}$. Johnson-Mehl tesselations can be seen as a sequential version of the Voronoï model, where the Poisson points are implanted sequentially with time. All classes grow then isotropically with the same rate, and the growth of crystal boundaries is stopped when they meet. All Poisson points falling in an existing crystal are removed.

From a mathematical viewpoint, a Johnson-Mehl tessellation is constructed from a sequential Poisson point process where the points $x_i, i = 1, .., N$ are implanted sequentially at a time $t_i, i = 1, .., N$. The classes $C_i, i = 1, .., N$ corresponding to the points $x_i, i = 1, .., N$ are defined by

$$C_i = \left\{ y \in \mathbb{R}^3, \forall j \neq i, t_i + \frac{\|x_i - y\|}{v} \leq t_j + \frac{\|x_j - y\|}{v} \right\}. \tag{9}$$

3.2.2 Exclusion Model

In our multiscale model, we rely now on a Johnson-Mehl tesselation to describe the exclusion polymer and its complementary: each class C_i is attributed to the exclusion polymer with the probability v_e ($= 0.2$ in the present case) and to the other polymer with the probability $1 - v_e$, generating a binary Johnson-Mehl mosaic (Figure 8 a), that allows us to preserve the symmetry between the geometry of the exclusion polymer and its complementary. Here, the two previous parameters of exclusion zone model (R_e and θ_e) are replaced by a single one, namely the intensity θ_e of the Poisson point process associated to the Johnson-Mehl tesselation. The remaining parts of the model are the same as previously. Simulation parameters are the intensity of the Poisson point processes attached to each polymer.

A realization of the Johnson-Mehl based model is displayed in Figure 8, as an illustrative example. A vectorial simulation of a domain with a $1\mu m^3$ volume is generated in 10 minutes.

The overall construction of the model is summarized in Figure 9.

If the volume fraction v_e of exclusion polymer and the radius R_{cb} of the carbon black particles are known, the global model is controlled by the following set of parameters:

- the intensity θ_e of the Poisson point process associated to the Johnson-Mehl tesselation
- the intensity θ_a of the Poisson point process on which relies the modelling of the aggregates,
- the radius R_a of the boolean spheres used to model the aggregates,
- the intensity θ_{cb} of the Cox point process on which relies the modelling of the spatial distribution of the black carbon particles.

Finally, the bound rubber is obtained as before by considering the Boolean difference of a Boolean model of sphere of constant radius $R_{cb} + t$ implanted on the centers of the black carbon particles and of the Boolean spheres describing the black carbon particles.

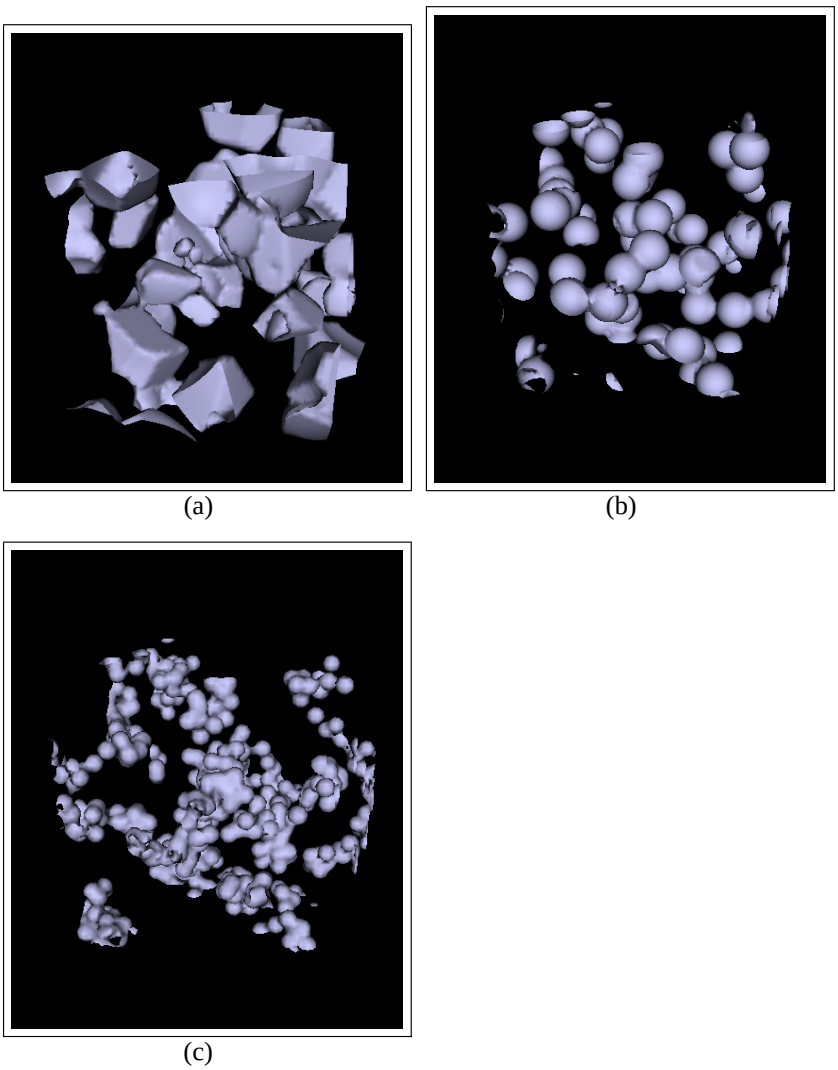

Figure 8: The three steps of the construction of the model: (a) exclusion polymer (Johnson-Mehl mosaic); (b) aggregates; (c) carbon black particles network ($v_e = 0.2$; $\theta_e = 4.10^{-7}$ nm^{-3}; $R_a = 60$ nm; $R_{cb} = 20$ nm; simulated volume: (500 nm)^3)

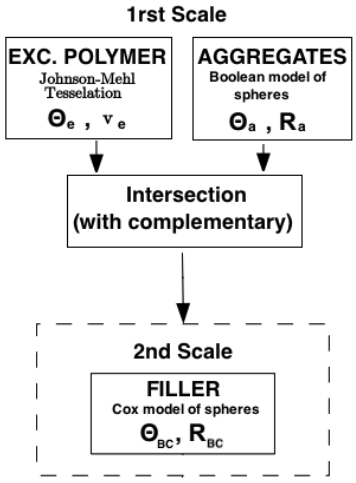

Figure 9: Scheme of the multiscale random model (exclusion polymer made of a Johnson-Mehl mosaic)

3.2.3 Model Ffitting from Experimental Data

As previously, the parameters of the Johnson-Mehl exclusion model are estimated to match the morphological descriptors obtained on the experimental TEM images. The values of the parameters obtained after optimization are given in the Table 2. The experimental covariance and granulometry are compared with the corresponding curves obtained by the simulations with fitted parameters on Figure 10. It turns out that the agreement between experimental data and measurements made on simulations is better than in the previous version of the model. A simulated image is shown in Figure 11 and compared to a TEM image.

v_e	θ_e (nm$^{=3}$)	θ_a (nm^{-3})	R_a (nm)	θ_{cb} (nm^{-3})	R_{cb} (nm)
0.2	4.0×10^{-7}	4.0×10^{-7}	60	3.5×10^{-5}	18

Table 2: Optimized parameters for the Johnson-Mehl model of exclusion polymer

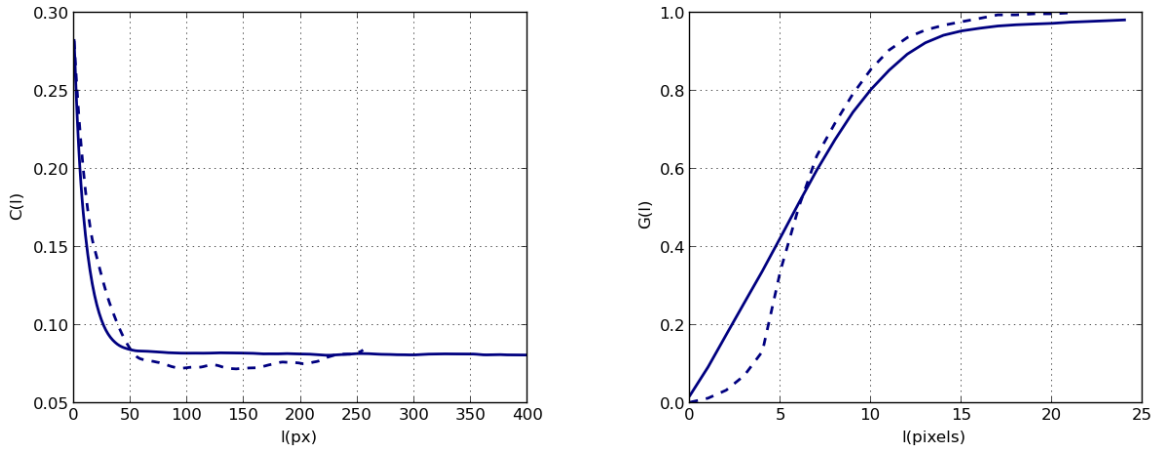

(a) (b)

Figure 10: Covariance (a) and granulometry (b) of the simulated material (Johnson-Mehl mosaic for the exclusion polymer). The simulated curves are represented by the discontinuous lines, the experimental curves by the continuous lines.

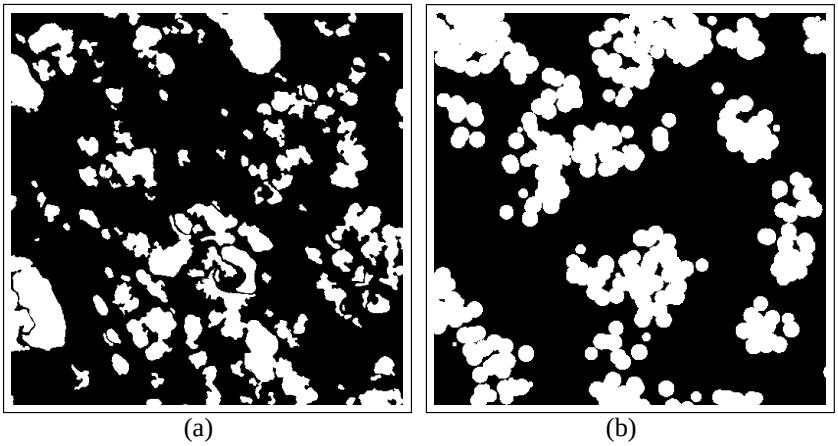

(a) (b)

Figure 11: Comparison between an experimental (a) and a simulated TEM image (b) for the Johnson-Mehl mosaic model of exclusion polymer.

3.3 Implementation of the Models

Simulations of random structures are generally performed on a grid of points (i.e. 2D or 3D images), using primary grains based on combination of pixels. The implementation in the software VtkSim relies on a completely different approach based upon level sets and implicit functions. In this approach, primary grains are described by implicit functions (Faessel and Jeulin (2011); Faessel (2012)), which are real valued functions defined in the 3D space. The level sets of an implicit function Φ are described by an equation of the form $\Phi(x, y, z) = c$, for some constant c. A surface is described as a level set of the function Φ, most commonly the set of points for which $\Phi(x, y, z) = 0$. In this case, the points for which $\Phi(x, y, z) < 0$ correspond to the interior of the primary grain associated to the implicit function, the points for which $\Phi(x, y, z) > 0$ to its complementary and the level set $\Phi(x, y, z) = 0$ to the boundary of the primary grain. Any primary grain can be implemented, whatever its shape, as long as it can be represented using an implicit function.

In the implicit function approach, complete simulations are generated, using Boolean combinations of primary implicit functions: the union and the intersection of two objects A_1 and A_2 are defined to yield the minimum and the maximum, respectively, of their corresponding implicit functions. Thus, we have

$$\Phi(A_1 \cup A_2) = \min\{\Phi(A_1), \Phi(A_2)\} \tag{10}$$

and

$$\Phi(A_1 \cap A_2) = \max\{\Phi(A_1), \Phi(A_2)\}. \tag{11}$$

Similarly, the complementary A^c of set A is defined to be the opposite function

$$\Phi(A^c) = -\Phi(A). \tag{12}$$

Several classical random models can be generated using this method, including among others soft-core or hard-core Boolean models of spheres. Interestingly, since a combination of implicit functions is itself an implicit function, the realization of a first random simulation enables us to generate multiscale simulations. An interesting feature of the software is that it allows to directly export the simulated microstructures as a mesh for further use, like finite elements based computations. Overall, using implicit functions to perform the simulation allows us to build complex combinations of simulations that we could not process with a pixel based method. Furthermore, vectorial simulations do not require a large amount of computer resources, which allows us to obtain fast generations of microstructures with very large sizes and numbers of primary grains.

4 Percolation of the Carbon Black Network

It is known that there is a large impact of the connectivity of elements in a random system on its macroscopic behavior. Controlling the percolation of a network is of major interest in the optimization of the microstructure. In this section, we focus on the percolation of the clusters constituted by the filler particles. Percolating networks of filler can indeed significantly change the mechanical properties of the material. It is therefore of interest to be able to select simulation parameters that will (or not) create percolating paths in the material.

4.1 General Approach

A simulation is said to percolate when a continuous path can be drawn in the filler phase that connects two opposite faces of the simulation window (a cube in the 3D space). Our aim is to determine the probability p that a simulation in a cubic window of length L percolates. To estimate p, N simulations of the random model are performed, and the number of simulations that percolate is recorded. A set of parameters leads to a percolating medium when more than 50 percents of the simulations percolate. In this approach, p is estimated by

$$\hat{p}_N = \frac{1}{N} \sum_{n=1}^{N} P_k, \tag{13}$$

where P_k is the random variable equal to 1 when the simulation percolates and 0 otherwise. The estimator $\hat{p}_N$ is without bias. We denote by $\sigma^2 = p(1-p)$ the variance of the random variables $\{P_i, i = 0, .., N\}$. The variance of $\hat{p}_N$ is then given by

$$\text{Var}(\hat{p}_N) = \frac{\sigma^2}{N}. \tag{14}$$

Hence, $\text{Var}(\hat{p}_N) \to 0$ when $N \to +\infty$ and the estimator $\hat{p}$ converges. For N large enough, according to the Central Limit Theorem, we have

$$\hat{p}_N \sim \mathcal{N}(p, \sigma^2/N), \tag{15}$$

where $\mathcal{N}(p, \sigma^2/N)$ denotes the normally distributed law with mean p and standard deviation $\sigma/\sqrt{N}$. Therefore, it can be show that, for $N = 100$, with confidence 95%,

$$p - 1.96\sqrt{\frac{p(1-p)}{N}} \leq \hat{p} \leq p + 1.96\sqrt{\frac{p(1-p)}{N}}. \tag{16}$$

Since the quantity $p(1-p)$ is maximal for $p = 1/2$, yielding $p(1-p) = 1/4$, we have, in the worst case,

$$p - 0.098 \leq \hat{p} \leq p + 0.098. \tag{17}$$

In mathematical terms, we have

$$\mathbb{P}\Big\{p - 0.098 \leq \hat{p} \leq p + 0.098\Big\} \geq 0.95. \tag{18}$$

This result provides an estimation of the precision of the results obtained in the percolation study.

4.2 Percolation Algorithm

The aim of the percolation algorithm is to label the connected clusters of filler particles. For each connected cluster, it is then determined if it is percolating. The percolation algorithm proceeds as follows:

1. A realization of the model is simulated in a volume of fixed size. At the end of the simulation, the algorithm returns a list of the coordinates of the filler particles centers.
2. Following the approach of Moreaud and Jeulin (2005), the volume is subdivided into cubes of size R, R being the radius of the filler particle. The coordinates of the filler particles centers are then sorted according to the subvolumes.
3. The classical two-pass algorithm is used to label all clusters of filler particles. For a given particle, the number of test of intersection is restricted to the adjacent cubes, thus yielding a fast method of construction.
4. For each labelled cluster, the algorithm checks if the cluster is percolating.

4.3 Results

The effect of various morphological parameters on the proportion of percolating simulations, estimated on 100 realizations for each set of parameters, was investigated for the two previous models of multiscale random microstructures: volume fraction of filler, size of aggregates, size of the exclusion polymer clusters. Two sizes of simulations were used, namely (400 nm)^3 and (800 nm)^3. We report here results obtained on the largest simulations.

Volume fraction of fillers The volume fraction of fillers is controlled in the simulations by means of the intensity θ_{cb} for the centers of the carbon black spheres. The remaining parameters of the simulations are as follows: $v_e = 0.2$; $R_e = 30$ nm (Boolean model for the exclusion polymer), $\theta_e = 4.0 \times 10^{-7}\text{nm}^{-3}$ (Johson-Mehl mosaic); $v_a = 0.47$; $R_a = 60$ nm; $R_{cb} = 18$ nm; simulated volume: (800 nm)^3. The effect of θ_{cb} is illustrated by Figure 12. From these results, it turns out that the percolation threshold p_c (i.e. the lowest value of p for which more than 50% of realizations percolate) is given by $v_{cb} = 0.15$ for the Boolean model of exclusion and by $v_{cb} = 0.16$ for the Johnson-Mehl mosaic. Therefore, the second model shows a slightly higher percolation threshold. Since the nominal carbon black volume fraction of the real material is $v_{cb} = 0.14$, it is expected that its filler network does not percolate, which prevent the material to show a rigid macroscopic behavior.

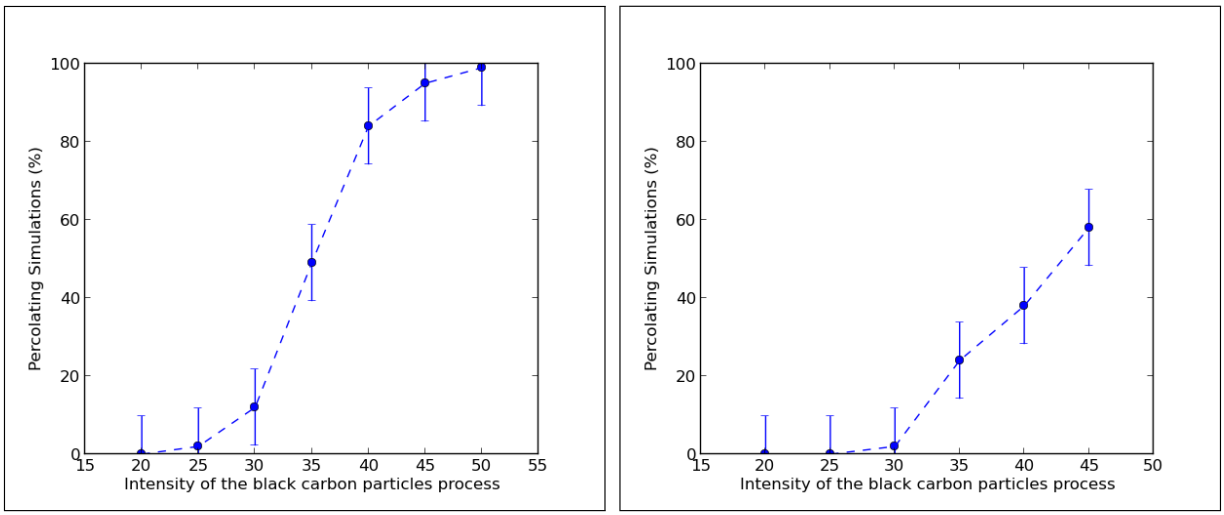

(a) (b)

Figure 12: Influence of the density θ_{cb} of filler (for V_e and V_a fixed) on the proportion of percolating simulations for the two models of exclusion zones: (a) Boolean model of spheres; (b) Johnson-Mehl mosaic. Simulated volume: (800 nm)^3

Aggregates size The effect of the size R_{aggr} of the filler aggregates of the material was studied, while keeping constant the volume fraction of aggregates. We remind that the volume fraction of aggregates is given by

$$v_a = (1 - v_e)\left(1 - \exp(-\theta_i \frac{4\pi}{3} R_i^3)\right). \tag{19}$$

By properly varying the intensity θ_{aggr}, the volume fraction of aggregates remains constant. The simulation parameters are $v_e = 0.2$, $R_e = 30$ nm (Boolean model), , $\theta_e = 4.0 \times 10^{-7}\text{nm}^{-3}$ (Johnson-Mehl mosaic); $v_a = 0.47$; $\theta_{cb} = 3.5 \times 10^{-5}$ nm^{-3}, $v_{cb} = 0.14$ and $R_{cb} = 18$ nm.

The results are displayed in Figure 13. Interestingly, we note that, all things otherwise equal, increasing the size of the aggregates results in a monotonous increase of the percentages of simulations that percolate. For instance the percentage of percolating simulations climbs from 40 percents when $R_{aggr} = 55$ nm to 60 percents when $R_{aggr} = 70$ nm for the two types of models, so that percolation in enhanced for larger aggregates.

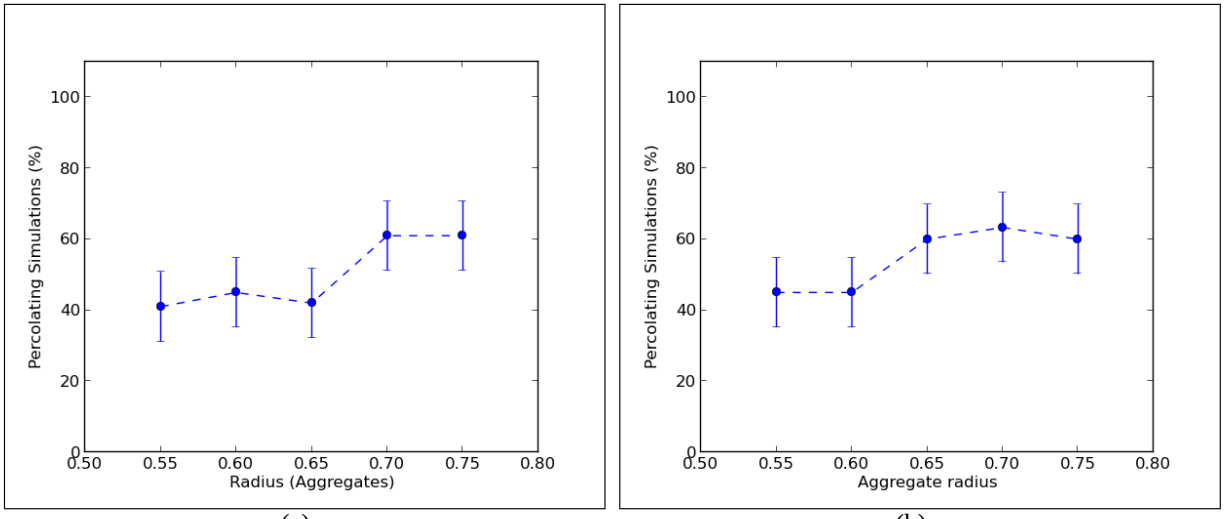

(a) (b)

Figure 13: Influence of the aggregates size (with V_e, V_a and v_{cb} fixed) on the proportion of percolating simulations for the two models of exclusion zones: (a) Boolean model of spheres; (b) Johnson-Mehl mosaic. Simulated volume: $(800\ \text{nm})^3$

Exclusion polymer clusters size From simulations generated by variations of the intensity θ_e of the Poisson point process, the number of exclusion polymer clusters increases (and thus their size is reduced since the volume fraction of exclusion polymer is kept constant). It results in a very slight decrease of the number of percolating simulations for both models. Overall, the effect of the exclusion polymer clusters size on percolation properties remains rather small.

5 Prediction of Viscoelastic Properties of simulated 3D Microstructures by Fast Fourier Transform (FFT)

5.1 Introduction

In this section a preliminary study of the viscoelastic behavior of the models of random microstructure is presented. For simplicity, the approach is restricted to the case of two-components media, namely a viscoelastic matrix and an elastic filler. In the present, accordingly, the mechanical behavior of the various polymers (exclusion polymer, polymer containing the filler, thin layer around carbon-black particles) is supposed to be the same. In addition, only small deformations of the polymer are considered.

Using a Fourier decomposition in time, strain and stresses are specified as a series of harmonics. This is commonly accounted for by the introduction of complex elastic moduli. A Fourier decomposition in space is introduced, making use of FFT methods to compute the elastic response of highly-contrasted composites. This method is first validated using analytical results for periodic media and compared with explicit time-discretization. It is efficiently applied to arbitrarily complex microstructures provided by a regular grid of voxels, such as images of real or of simulated microstructures, and does not require any further meshing of images. Extended to the viscoelastic case, it provides full-field reconstructions in time-space, from which the effective viscoelastic properties of a composite medium are estimated.

In what follows, a complex FFT scheme for viscoelastic composites is introduced and applied to 3D simulations of the two previously introduced versions of the multiscale model.This section presents a complex Fourier (FFT) scheme for computing the viscoelastic response of composites. Linear strain-stress relations with elastic and viscoelastic phases are considered. The problem to solve is presented in Section (5.2). The FFT method used to solve the problem is described in Section (5.3). It is validated in Section (5.4) and used to predict the properties of rubber containing fillers in Section (5.5).

5.2 Problem Setup

Consider a domain V representing a heterogeneous material subject to steady-state oscillatory conditions. In the harmonic regime, the time-dependence of the strain $\widetilde{\boldsymbol{\varepsilon}}$ and stress fields $\widetilde{\boldsymbol{\sigma}}$ at point $\mathbf{x}$ is given by the complex fields:

$$\widetilde{\boldsymbol{\varepsilon}}(\mathbf{x};t) = \boldsymbol{\varepsilon}(\mathbf{x})\, e^{i\omega t}, \qquad \widetilde{\boldsymbol{\sigma}}(\mathbf{x};t) = \boldsymbol{\sigma}(\mathbf{x})\, e^{i\omega t}, \tag{20}$$

where the amplitudes $\boldsymbol{\varepsilon}$ and $\boldsymbol{\sigma}$ are second-rank tensor fields, and ω is the frequency applied to the system. In the above, $\boldsymbol{\varepsilon}(\mathbf{x})$ and $\boldsymbol{\sigma}(\mathbf{x})$ are complex and do not depend on the time t. The physical strain and stress fields are the real parts of $\widetilde{\boldsymbol{\varepsilon}}$ and $\widetilde{\boldsymbol{\sigma}}$:

$$\widehat{\boldsymbol{\varepsilon}}(\mathbf{x};t) = \mathcal{R}\left[\widetilde{\boldsymbol{\varepsilon}}(\mathbf{x};t)\right], \quad \widehat{\boldsymbol{\sigma}}(\mathbf{x};t) = \mathcal{R}\left[\widetilde{\boldsymbol{\sigma}}(\mathbf{x};t)\right]. \tag{21}$$

For simplicity, it is assumed that the material contains elastic inclusions (phase $\alpha = 2$) embedded in a viscoelastic matrix (phase $\alpha = 1$). Referring to $\mathbb{C}_2$ as the inclusions's isotropic elastic stiffness tensor, we have, in phase 2

$$\widetilde{\boldsymbol{\sigma}}(\mathbf{x};t) = \mathbb{C}_2 : \widetilde{\boldsymbol{\varepsilon}}(\mathbf{x};t), \quad \boldsymbol{\sigma}(\mathbf{x}) = \mathbb{C}_2 : \boldsymbol{\varepsilon}(\mathbf{x}), \tag{22}$$

or equivalently,

$$\sigma_{kk}(\mathbf{x}) = 3\kappa_2 \varepsilon_{kk}(\mathbf{x}), \quad \boldsymbol{\sigma}'(\mathbf{x}) = 2\mu_2 \boldsymbol{\varepsilon}'(\mathbf{x}). \tag{23}$$

where μ_2 is the inclusion's shear modulus, κ_2 its bulk modulus, and where the strain and stress deviatoric parts are defined as:

$$\varepsilon'_{ij} = \varepsilon_{ij} - (\varepsilon_{kk}/3)\delta_{ij}, \quad \sigma'_{ij} = \sigma_{ij} - (\sigma_{kk}/3)\delta_{ij}, \tag{24}$$

δ being the Kronecker symbol. Inclusions are embedded in a viscoelastic matrix, where the local strain-stress relation is written generally as

$$\widetilde{\boldsymbol{\sigma}}(\mathbf{x};t) = \int_{-\infty}^{t} \mathrm{d}\tau\, \mathbb{C}_1(t-\tau) : \frac{\mathrm{d}\widetilde{\boldsymbol{\varepsilon}}(\mathbf{x};\tau)}{\mathrm{d}\tau}. \tag{25}$$

In the above, $\mathbb{C}_1(t)$ designates a time-dependant fourth-order isotropic tensor with shear and bulk (strain-rate) moduli $\mu_1(t)$ and $\kappa_1(t)$. Following Christensen (2012) the time-dependence is removed using Eq. (20)

$$\sigma_{kk}(\mathbf{x}) = 3\kappa_1^*(i\omega)\varepsilon_{kk}(\mathbf{x}), \quad \boldsymbol{\sigma}'(\mathbf{x}) = 2\mu_1^*(i\omega)\boldsymbol{\varepsilon}'(\mathbf{x}), \tag{26}$$

for $\mathbf{x}$ in the matrix. The complex elastic moduli $\kappa_1^*(i\omega)$ and $\mu_1^*(i\omega)$ are

$$\kappa_1^*(i\omega) = \overline{\kappa_1} + i\omega \int_0^\infty \mathrm{d}\eta\, \left[\kappa_1(\eta) - \overline{\kappa_1}\right] e^{-i\omega\eta}, \tag{27a}$$

$$\mu_1^*(i\omega) = \overline{\mu_1} + i\omega \int_0^\infty \mathrm{d}\eta\, \left[\mu_1(\eta) - \overline{\mu_1}\right] e^{-i\omega\eta}, \tag{27b}$$

with

$$\overline{\kappa} = \lim_{t\to\infty} \kappa_1(t) \geq 0, \qquad \overline{\mu} = \lim_{t\to\infty} \mu_1(t) \geq 0. \tag{28}$$

The local response of the material is given by Eqs. (23) and (26). Viscous effects are taken into account by the imaginary parts of the elastic moduli $\mu_1(i\omega)$ and $\kappa_1(i\omega)$. When the latter are positive, the stress fields's oscillations are advanced by an amount of

$$\Delta t = \frac{\arg\left[\boldsymbol{\sigma}(\mathbf{x})\right] - \arg\left[\boldsymbol{\varepsilon}(\mathbf{x})\right]}{\omega}, \tag{29}$$

compared to that of the strain field. For instance, if $\boldsymbol{\varepsilon}(\mathbf{x})$ is real

$$\widetilde{\boldsymbol{\sigma}}(\mathbf{x};t) = \mathcal{R}\left[\boldsymbol{\sigma}(\mathbf{x})\right]\, e^{i\omega(t-\Delta t)}. \tag{30}$$

Such effects are absent in the purely elastic case (23).The material equations above are completed by admissibility equations for the strain and stress fields. Assuming first that the displacement field $\mathbf{u}(\mathbf{x};t)$ is infinitesimal compared to the microstructure characteristic sizes, we have

$$\widetilde{\varepsilon}_{ij}(\mathbf{x};t) = \frac{\partial_j \widetilde{u}_i(\mathbf{x};t) + \partial_i \widetilde{u}_j(\mathbf{x};t)}{2}. \tag{31}$$

Second, stress equilibrium is met at every point

$$\partial_i \widetilde{\sigma}_{ij}(\mathbf{x};t) = 0. \tag{32}$$

We define the complex displacement amplitude $\mathbf{u}(\mathbf{x})$ by

$$\widetilde{\mathbf{u}}(\mathbf{x};t) = \mathbf{u}(\mathbf{x})\, e^{i\omega t} \tag{33}$$

so that Eqs. (31) and (32) become

$$\varepsilon_{ij}(\mathbf{x}) = \frac{\partial_j u_i(\mathbf{x}) + \partial_i u_j(\mathbf{x})}{2}, \quad \partial_i \sigma_{ij}(\mathbf{x}) = 0. \tag{34}$$

Applying periodic boundary conditions with time-harmonic macroscopic strain loading as

$$\langle \widetilde{\boldsymbol{\varepsilon}}(\mathbf{x};t)\rangle = \overline{\boldsymbol{\varepsilon}}\, e^{i\omega t}, \quad \widetilde{\boldsymbol{\varepsilon}}(\mathbf{x};t)\,\#, \quad \widetilde{\boldsymbol{\sigma}}(\mathbf{x};t)\,\#, \tag{35}$$

where $\overline{\boldsymbol{\varepsilon}}$ is a constant, $\langle\cdot\rangle$ designates a spatial average over the domain V and $\#$ denotes a periodic field in space with elementary cell V. The above is indifferently written as

$$\langle \boldsymbol{\varepsilon}(\mathbf{x})\rangle = \overline{\boldsymbol{\varepsilon}}, \quad \boldsymbol{\varepsilon}(\mathbf{x})\,\#, \quad \boldsymbol{\sigma}(\mathbf{x})\,\#. \tag{36}$$

Hereafter it is assumed, without loss of generality, that all components of $\overline{\boldsymbol{\varepsilon}}$ are real. The composite's effective response is given by the stiffness tensor $\mathbb{C}^{eff}$

$$\overline{\boldsymbol{\sigma}} = \langle \boldsymbol{\sigma}(\mathbf{x})\rangle = \mathbb{C}^{eff} : \overline{\boldsymbol{\varepsilon}}. \tag{37}$$

When the composite is isotropic and V is large enough, the tensor $\mathbb{C}^{eff}$ is isotropic as well. Its shear and bulk moduli are noted μ^{eff} and κ^{eff}.

Eqs. (23), (26), (34) and (36) define the response of the material to a harmonic solicitation. In theory, these solutions allow one to reconstruct the local and macroscopic responses of the material subjected to non-harmonic (arbitrary) strain loading, in the steady-state regime (Christensen (2012)). The first equation in (35) can be replaced by

$$\alpha(t) = \langle \widetilde{\boldsymbol{\varepsilon}}(\mathbf{x};t)\rangle, \tag{38}$$

so that a time-varying macroscopic strain loading $\alpha(t)$ is applied. Taking the Fourier transform of the latter

$$\alpha(t) = \frac{1}{2\pi}\int_{-\infty}^{\infty} \mathrm{d}\omega\, \alpha(\omega)\, e^{i\omega t}. \tag{39}$$

The strain field acting in the material is the superposition of the following harmonic responses

$$\widetilde{\boldsymbol{\varepsilon}}(\mathbf{x};t) = \frac{1}{2\pi}\int_{-\infty}^{\infty} \mathrm{d}\omega\, \boldsymbol{\varepsilon}_\omega(\mathbf{x})\, e^{i\omega t}, \tag{40}$$

where $\boldsymbol{\varepsilon}_\omega(\mathbf{x})$ is the complex field solution of Eqs. (23), (26), (34) and (36) with $\overline{\boldsymbol{\varepsilon}} = \alpha(\omega)$.

5.3 FFT Methods

The purpose of this section is to solve numerically Eqs. (23), (26), (34) and (36) on a grid of voxels, using "Fourier methods" as developed by Moulinec and Suquet (1994); Eyre and Milton (1999); Michel et al. (2001). The "direct

scheme" (Moulinec and Suquet (1994)) and "augmented Lagrangean" (Michel et al. (2001)) Fourier methods apply to linear elasticity. The "accelerated scheme" (Eyre and Milton (1999)), originally given in the context of conductivity, has been extended to linear elasticity by Michel et al. (2001) . We remark that the problem (23), (26), (34) and (36) is mathematically identical to that of linear elasticity, except that complex instead of real fields are concerned. Thus, FFT methods apply to the viscoelastic problem considered here, as will be seen later. This is true of other more recent FFT methods like the "rotated" scheme (Willot (2015)) and "variational FFT"(Brisard and Dormieux (2010)) schemes. Accordingly, any of these schemes can be implemented for this purpose.

Hereafter, the "discrete" scheme proposed by Willot and Pellegrini (2008), coupled with the algorithm of Moulinec and Suquet (1994), is used. A similar scheme has already been investigated in the context of conductivity by Willot et al. (2014) leading to much improved convergence properties, especially for highly-contrasted composites. The scheme gives for the k^{th}-iteration

$$\boldsymbol{\varepsilon}^{k+1}(\mathbf{q}) = \overline{\boldsymbol{\varepsilon}} - \mathbb{G}^0(\mathbf{q}) : \left[\boldsymbol{\sigma}(\mathbf{q}) - \mathbb{C}^0 : \boldsymbol{\varepsilon}^k(\mathbf{q})\right], \tag{41}$$

where $\mathbf{q}$ is the Fourier wave vector, $\mathbb{C}^0$ is a reference elastic tensor and $\mathbb{G}^0(\mathbf{q})$ its associated Green operator, discretized using a forward and backward finite difference scheme on the rotated grid. The stress field is computed at each step in the direct space using the material's constitutive law, and the strain field is initialized by $\boldsymbol{\varepsilon}^{k=0} \equiv \overline{\boldsymbol{\varepsilon}}$. Convergence strongly depends on $\mathbb{C}^0$, an arbitrary (complex) reference tensor, which has to be optimized. An absolute convergence criterion is defined on stress equilibrium as

$$\max_{\mathbf{x}} |div\boldsymbol{\sigma}(\mathbf{x})| \leq \eta \tag{42}$$

where η is the required precision. Care is needed when choosing $\mathbb{C}^0$. To ensure that the physical strain and stress fields are symmetric, i.e.

$$\widehat{\varepsilon}_{kl}(\mathbf{x};t) = \widehat{\varepsilon}_{lk}(\mathbf{x};t), \quad \widehat{\sigma}_{kl}(\mathbf{x};t) = \widehat{\varepsilon}_{lk}(\mathbf{x};t), \tag{43}$$

it is necessary to enforce:

$$\varepsilon_{kl}(\mathbf{x}) = \varepsilon_{lk}(\mathbf{x}), \quad \sigma_{kl}(\mathbf{x}) = \sigma_{lk}(\mathbf{x}). \tag{44}$$

Hence, the tensors $\boldsymbol{\varepsilon}$ and $\boldsymbol{\sigma}$ are not symmetric in the complex sense. To enforce this, the Green tensor must satisfy

$$G^0_{ij,kl}(\mathbf{q}) = G^0_{ji,kl}(\mathbf{q}) = G^0_{ij,lk}(\mathbf{q}) = \left[G^0_{kl,ij}(\mathbf{q})\right]^* . \tag{45}$$

In turn, this implies

$$C^0_{ij,kl} = C^0_{ji,kl} = C^0_{ij,lk} = \left(C^0_{kl,ij}\right)^* = C^0_{kl,ij}, \tag{46}$$

so that $\mathbb{C}^0$ must be real. This is in contrast with optics where we are free to choose complex references (see Azzimonti et al. (2013)). In the rest of this work, we choose $\kappa^0 = 0.51\,[Re(\kappa_1^*) + Re(\kappa_2^*)]$, $\mu^0 = 0.51\,[Re(\mu_1^*) + Re(\mu_2^*)]$, for the bulk and shear moduli of the reference tensor, respectively, where $\mu^*_{1,2}$, $\kappa^*_{1,2}$ are the complex elastic moduli in phases 1 and 2.

5.4 Validation and Comparison with an Explicit Time-discretized FFT Scheme

In this section, a periodic array of spheres with cubic symmetry is considered. The spheres are purely elastic with shear and bulk moduli $\mu_2 = \kappa_2 = 1000$ GPa, and, for simplicity, the embeding medium is supposed to be Maxwellian. Outside the spheres, the stress $\sigma(t)$ and strain fields $\varepsilon(t)$ satisfy

$$\frac{\widetilde{\sigma'}(t)\mathrm{d}t}{t_1} + \mathrm{d}\widetilde{\sigma'}(t) = 2\mu_0 \mathrm{d}\widetilde{\varepsilon'}(t), \quad \frac{\widetilde{\sigma}_{kk}(t)\mathrm{d}t}{t_1} + \mathrm{d}\widetilde{\sigma}_{kk}(t) = 3\kappa_0 \mathrm{d}\widetilde{\varepsilon}_{kk}(t) \tag{47}$$

with $\mu_0 = \kappa_0 = 1$ GPa, $t_1 = 1$ s. This is equivalent to Christensen (2012)

$$\widetilde{\sigma'}(t) = \int_{-\infty}^{t} \mathrm{d}\tau\, 2\mu_1(t-\tau)\frac{\mathrm{d}\widetilde{\varepsilon'}(\tau)}{\mathrm{d}\tau}, \quad \widetilde{\sigma}_{kk}(t) = \int_{-\infty}^{t} \mathrm{d}\tau\, 3\kappa_1(t-\tau)\frac{\mathrm{d}\widetilde{\varepsilon}_{kk}(\tau)}{\mathrm{d}\tau}, \tag{48}$$

with

$$\mu_1(t) = \mu_0 \mathbf{e}^{-t/t_1}\mathcal{H}(t), \qquad \kappa_1(t) = \kappa_0 \mathbf{e}^{-t/t_1}\mathcal{H}(t), \qquad \mathcal{H}(t) = \left\{ \begin{array}{ll} 0 & \text{if } t < 0, \\ 1 & \text{if } t > 0. \end{array} \right. \tag{49}$$

In the above, $\mathcal{H}(t)$ is the Heaviside step function. Using (25) the complex elastic moduli in the embedding medium read, as functions of the angular frequency ω

$$\mu_1^*(\omega) = \frac{\mu_0}{1 + 1/(\omega t_1)}, \quad \kappa_1^*(\omega) = \frac{\kappa_0}{1 + 1/(\omega t_1)}. \tag{50}$$

Heareafter the frequency is set to $\omega = 1[rad/s]$. A sphere is discretized in a cubic domain of size $64 \times 64 \times 64$ voxels. The FFT method described in Sec. (5.3) is then used to solve the viscoelastic problem in the complex domain. The spheres composite has a macroscopic response with cubic symmetry of bulk moduli κ_s and shear moduli μ_p, μ_s

$$C = \begin{pmatrix} \kappa_s + \frac{4}{3}\mu_p & \kappa_s - \frac{2}{3}\mu_p & \kappa_s - \frac{2}{3}\mu_p & 0 & 0 & 0 \\ & \kappa_s + \frac{4}{3}\mu_p & \kappa_s - \frac{2}{3}\mu_p & 0 & 0 & 0 \\ & & \kappa_s + \frac{4}{3}\mu_p & 0 & 0 & 0 \\ & & & \mu_s & 0 & 0 \\ & \text{sym} & & & \mu_s & 0 \\ & & & & & \mu_s \end{pmatrix} \tag{51}$$

in Voigt notation where $\varepsilon = (\varepsilon_{xx}, \varepsilon_{yy}, \varepsilon_{zz}, 2\varepsilon_{yz}, 2\varepsilon_{xz}, 2\varepsilon_{xy})$ and $\sigma = (\sigma_{xx}, \sigma_{yy}, \sigma_{zz}, \sigma_{yz}, \sigma_{xz}, \sigma_{xy})$. FFT Results are compared to the analytical estimates in Cohen (2004) (Figure 14).

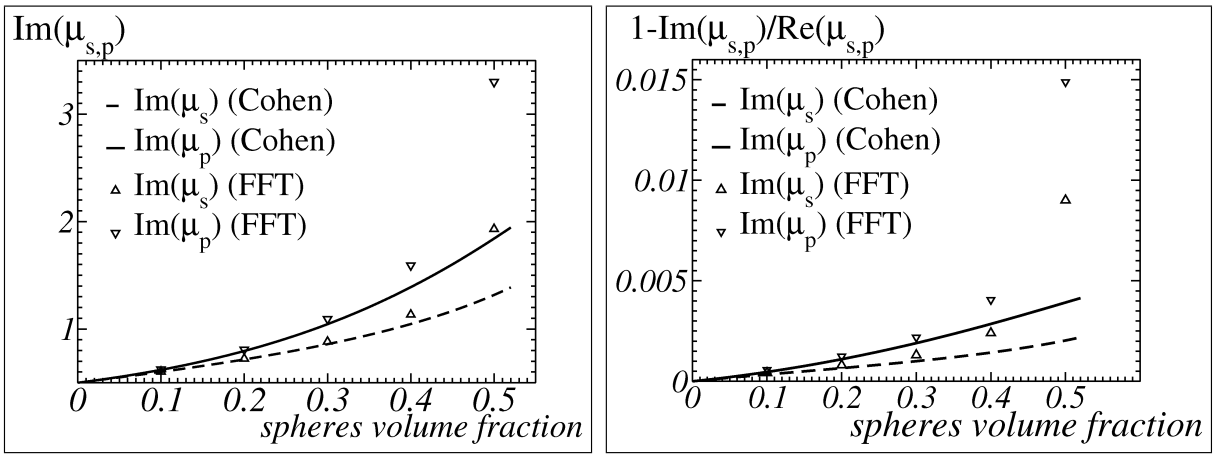

(a) (b)

Figure 14: Comparison between analytical estimates given by Cohen (2004) (solid and dashed lines) and FFT results (symbols) for the effective elastic response of a periodic array of spheres with varying volume fraction: imaginary part of the effective shear moduli $\mu_{p,s}$ (a) and ratio $\mathcal{I}m(\mu_{p,s})/\mathcal{R}e(\mu_{p,s})$.

Excellent agreement between the FFT results and analytical estimates is found for the complex shear moduli $\mu_{p,s}$ when the volume fraction of spheres is less than 20%. For the ratio $\mathcal{I}m(\mu_{p,s})/\mathcal{R}e(\mu_{p,s})$, good agreement is obtained for quite smaller volume fractions (not larger than 10%).

Finally, the Fourier method developed in Sec. (5.3) is compared to an explicit time-discretized scheme. Assume that

$$\widehat{\varepsilon}(\mathbf{x}; t) = 0, \qquad \widehat{\sigma}(\mathbf{x}; t) = 0 \tag{52}$$

for $t < t_0$. For $t \geq t_0$, the material is subject to harmonic strain loading

$$\langle \widehat{\varepsilon}(\mathbf{x}; t) \rangle = \cos(\omega t)\overline{\varepsilon} \tag{53}$$

Hereafter we take $t_0 = \pi/(2\omega)$ and again $\omega = 1$ [rad/s] for simplicity. The stress field σ at time $t + \mathrm{d}t$ is then computed by discretizing Eq. (47). For instance, for the deviatoric parts

$$\Delta\widehat{\sigma}\prime(\mathbf{x},t) = 2\mu^0\Delta\widehat{\varepsilon}\prime(\mathbf{x},t) - \frac{\widehat{\sigma}\prime(\mathbf{x},t)\Delta t}{t_1}, \qquad \Delta\widehat{\sigma}\prime(\mathbf{x},t) = \widehat{\sigma}\prime(\mathbf{x},t+\Delta t) - \widehat{\sigma}\prime(\mathbf{x},t), \tag{54}$$
$$\Delta\widehat{\varepsilon}\prime(\mathbf{x},t) = \widehat{\varepsilon}\prime(\mathbf{x},t+\Delta t) - \widehat{\varepsilon}\prime(\mathbf{x},t).$$

The above is mathematicaly equivalent to a thermoelastic stress-strain relation with unknown $\Delta\widehat{\varepsilon}$ and $\Delta\widehat{\sigma}$ and with applied strain loading given by (53)

$$\langle\Delta\widehat{\varepsilon}\prime(\mathbf{x},t)\rangle = -\omega\sin(\omega t)\Delta t\overline{\varepsilon} \tag{55}$$

In the inclusions, the fields $\Delta\widehat{\sigma}(\mathbf{x};t)$ and $\Delta\widehat{\varepsilon}(\mathbf{x};t)$ are related by Hooke's law. The FFT method for thermoelasticity proposed by Vinogradov and Milton (2008), Ambos et al. (2015) is then applied at each time step. We set $\Delta t = 0.01$ and apply shear loading with $\overline{\varepsilon_{12}} = \overline{\varepsilon_{21}} = 1$ and $\overline{\varepsilon_{ij}} = 0$ for $(i,j) \neq (1,2), (2,1)$. A comparison between the FFT scheme with time-discretized strain-stress relation and that with complex elastic moduli, is represented in Figure 15 for the macroscopic response. The macroscopic stress $\overline{\sigma_{12}} = \langle\sigma_{12}\rangle$ is given as a function of time t. It is emphasized that, for the time-discretized sheme, $\overline{\sigma_{12}}(t)$ (top dashed line) is computed at many loading step whereas, for the FFT method involving complex moduli one computation is carried out which gives the harmonic response at $t \to \infty$ (bottom dashed line). As expected, beyond an intermediary regime, the time-explicit scheme converges to a harmonic response identical to that predicted by the complex FFT scheme.

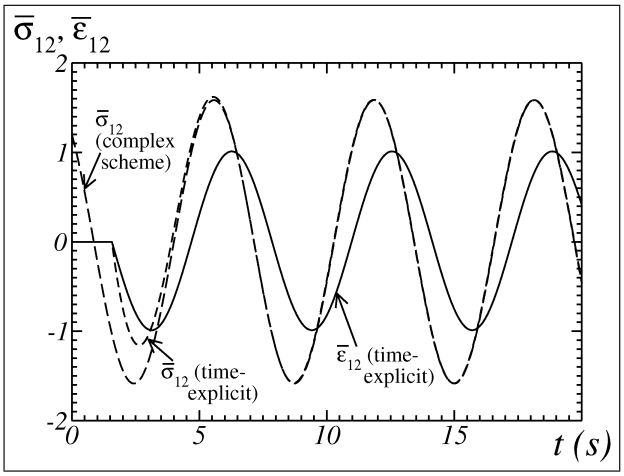

Figure 15: Macroscopic strain $\overline{\varepsilon}_{12} = \langle\widehat{\varepsilon}_{12}(\mathbf{x};t)\rangle$ and resulting stress component $\overline{\sigma}_{12} = \langle\widehat{\sigma}_{12}(\mathbf{x};t)\rangle$ vs. time t, for the time-discretized scheme. The macroscopic strain is 0 for $t < \pi/(2\omega)$. In violet: comparison with the harmonic regime as predicted by the complex Fourier scheme.

5.5 Computations on Random Two-scales Media

To illustrate the efficiency of the method, viscoelastic computations are performed on the Boolean and Johnson-Mehl two-scales models. The local properties are set to 78 400 and 30 000 MPa for the bulk and shear moduli, resp., in the filler. In the polymer, a viscoelastic law with Prony series given by Laiarinandrasana et al. (2012) is used. Complex elastic moduli are used for 23 frequencies. Each 3D computation required about 3 hours on a 12-cores computer and 800 iterations with $\eta = 3.10^{-5}$. No time discretization is used. Domains with size (0.8 μm)^3 discretized over (400)^3 voxels are simulated.

FFT maps of the mean stress field (opposite of pressure) are shown in Figure 16, showing a 2D section for the exclusion zones modelled by a Boolean model. The material is submitted to a hydrostatic strain loading, the frequency being $\omega = 117$ Hz. Strong internal stresses in the polymer appear in regions surrounded by fillers. Maps of the shear stress component with shear strain loading are shown in Figure 17.

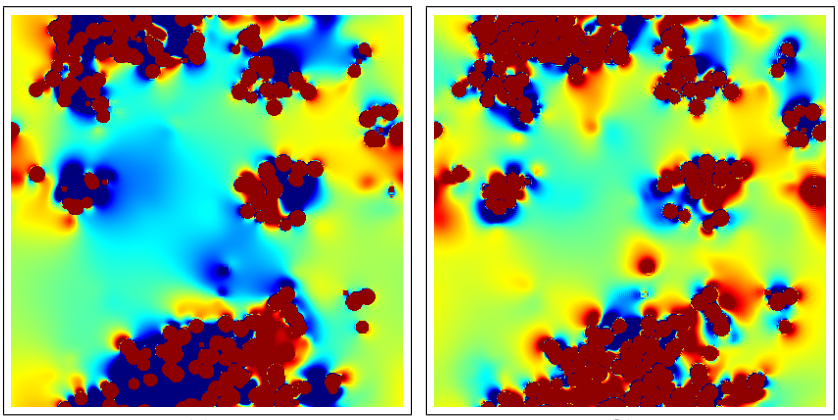

(a) (b)

Figure 16: Real and imaginary parts of the mean stress field σ_m for a hydrostatic strain loading ($\varepsilon_m = 1\%$) at a frequency $\omega = 117$ Hz. The minimal and maximal values are -47 and 140 Gpa (real part (a)) and -1.0 and 6.2 GPa (imaginary part (b)). The stress values are thresholded between 8.68 and 8.73 GPa (real part) and 1.5 and 1.6 (imaginary part) to highlight the field patterns in the polymer.

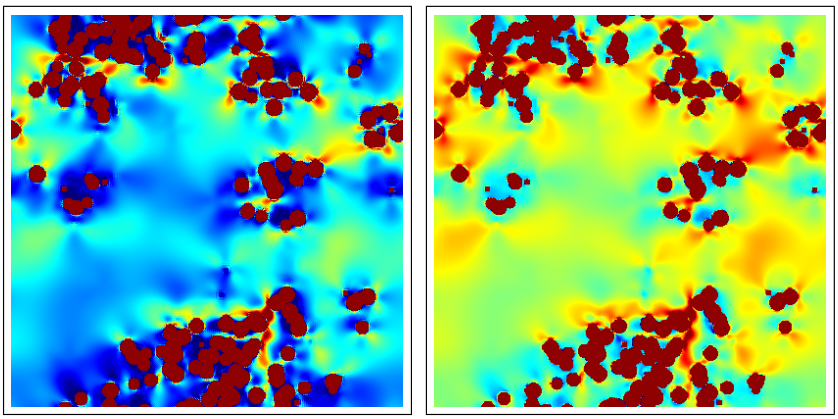

(a) (b)

Figure 17: Real and imaginary parts of the shear stress field σ_{12} for a shear strain loading ($\varepsilon_{xy} = 1\%$) at a frequency $\omega = 117$ Hz. The minimal and maximal values are -17 and 44 GPa (real part (a)) and -1.2 and 0.7 GPa (imaginary part (b)). The stress values are thresholded between 0 and 6 MPa (real part) and 0 and 1 (imaginary part) to highlight the field patterns in the polymer.

The effective moduli are obtained by averaging the fields calculated by FFT, using a standard homogenization approach. The relative precision of the estimated moduli is calculated from the variance of the fields at different scales, as developed in the statistical RVE approach of Kanit et al. (2003). At a frequency $\omega = 117$ Hz, the relative precision for the real part and the imaginary part of the bulk modulus is equal to 0.2% and to 0.3%. For the the real part and the imaginary parts of the shear modulus, it is equal to 17% and 3.8% respectively.

The frequency dependence of the effective complex bulk modulus and of the effective shear modulus are illustrated in Figures 18 and 19. FFT data for the Boolean and Johnson-Mehl models are compared to the viscoelastic response of the Hashin sphere assemblage (Hashin (1970)). The inner spheres and outer layers in the Hashin coating have the same properties as the fillers and polymer respectively, and the volume fraction are the same as in the model (about 10.6%). It has been shown that the bulk and shear moduli of isotropic two-phases viscoelastic composites are constrained to a region in the complex plane (Gibiansky and Milton (1993), Milton and Berryman (1997)) that generalizes the Hashin and Shtrikman bounds. The Hashin coating has extremal properties for the bulk modulus in the sense that its bulk modulus lies on the frontier of the region. For the material considered here, the contrast of properties in terms of bulk moduli is moderate (about 25), and so the Hashin coating is very close to that of the Boolean and Johnson-Mehl models, as computed using FFT (Figure 18). The situation is sensibly different for the real part of the shear modulus, which is 3.10^4 higher in the filler than in the polymer (Fig. 19 a). The real part of the shear modulus of the Johnson-Mehl model is higher than that of the Boolean model.

We note that the viscoelastic response of the models is much softer than that of the Hashin assemblage with stiff outer coating, which is not represented in Figs. 18 and 19. Our results are also consistent with that obtained by (Jean et al. (2011b)) in the context of elasticity, where elastic moduli close to the Hashin and Shtrikman lower bounds were predicted.

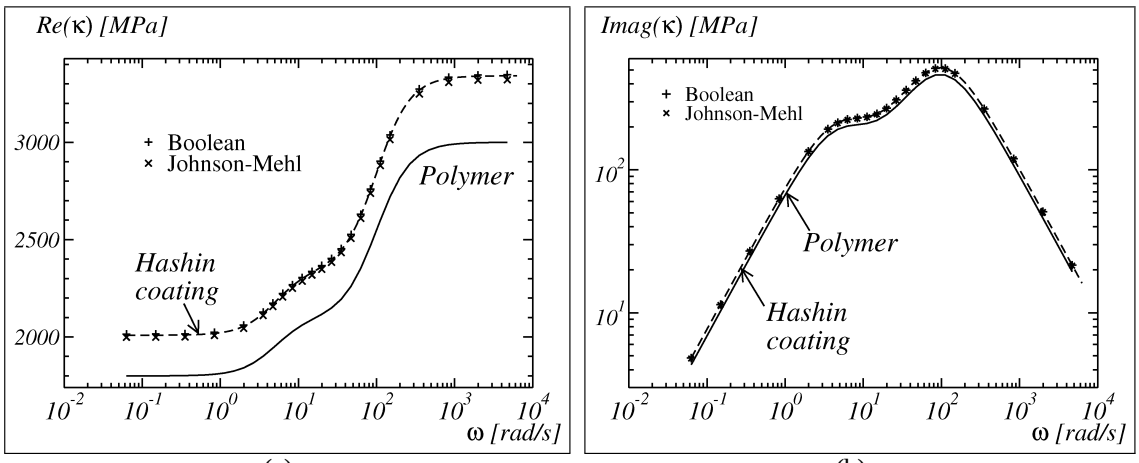

Figure 18: Comparison between the Johnson-Mehl and Boolean sphere models for the exclusion polymer and Hashin sphere assemblage: frequency dependence of the effective real part (a) and imaginary part (b) of the complex bulk modulus.

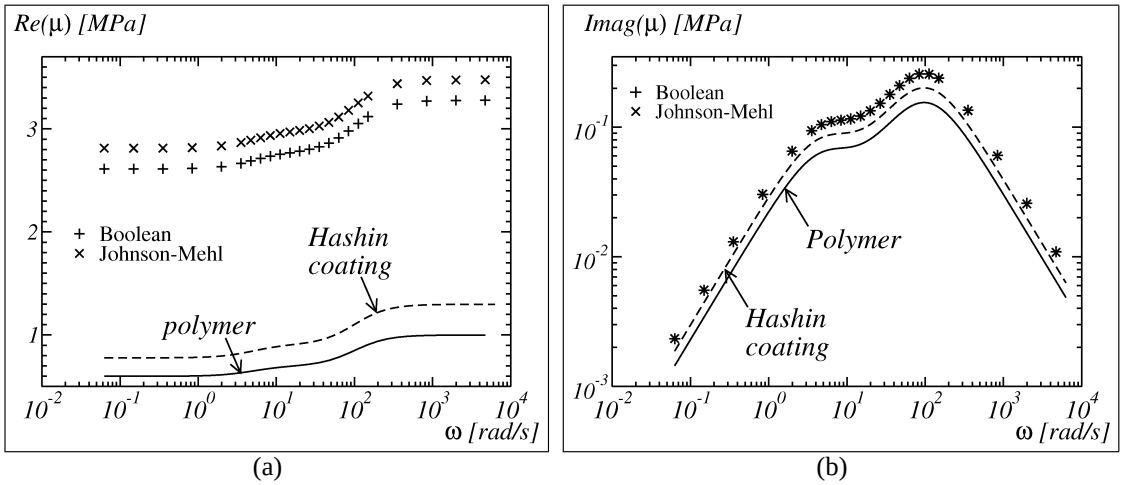

Figure 19: Continuation of Figure 18: frequency dependence of the effective real part (a) and imaginary part (b) of the complex shear modulus.

6 Conclusion

Multiscale morphological models of random 3D microstructures were developed to simulate the distribution of fillers in rubber materials, accounting for the presence of aggregates and of an exclusion polymer. These models enable us to study the percolation of carbon black filler as a function of its multiscale distribution. It was proved that the two models involving a different morphology for the exclusion polymer do not percolate for the volume fraction of carbon black contained in the material.

The effective viscoelastic moduli are predicted by Fast Fourier Transforms on 3D simulated images of the microstructure. The simple method proposed in this work predicts the harmonic response of composites with arbitrary microstructures, frequency per frequency and is restricted to linear materials. The effective bulk modulus and shear modulus are predicted in a large frequency range (about from 10^{-1} to 10^{4} rad/s).

Further studies will involve a systematic change of the microstructures by means of the parameters of the model,

and its impact on the effective properties, to find optimal microstructures with respect to the macroscopic behavior.

Acknowledgements: F. Willot is indebted to S. Forest for helpful suggestions regarding the FFT-based computations.

References

Ambos, A.; Willot, F.; Jeulin, D.; Trumel, H.: Numerical modeling of the thermal expansion of an energetic material. *International Journal of Solids and Structures*, 60-61, (2015), 125–139.

Azzimonti, D.; Willot, F.; Jeulin, D.: Optical properties of deposit models for paints:full-fields FFT computations and representative volume element. *Journal of Modern Optics*, 60, 7, (2013), 519–528.

Bergström, M. C., J. S .and Boyce: Constitutive modeling of the large strain time-dependent behavior of elastomers. *Journal of the Mechanics and Physics of Solids*, 46, 5, (1998), 931–954.

Brisard, S.; Dormieux, L.: FFT-based methods for the mechanics of composites: A general variational framework. *Computational Materials Science*, 49, 3, (2010), 663–671.

Christensen, R.: *Theory of viscoelasticity: an introduction*. Elsevier (2012).

Cohen, I.: Simple algebraic approximations for the effective elastic moduli of cubic arrays of spheres. *Journal of the Mechanics and physics of Solids*, 52, 9, (2004), 2167–2183.

Delarue, A.; Jeulin, D.: 3d morphological analysis of composite materials with aggregates of spherical inclusions. *Image Anal Stereol*, 22, (2003), 153–161.

Eyre, D.; Milton, G.: A fast numerical scheme for computing the response of composites using grid refinement. *The European Physical Journal Applied Physics*, 6, 1, (1999), 41–47.

Faessel, M.: Vtksim software. http://cmm.ensmp.fr/ faessel/vtkSim/demo/ (2012).

Faessel, M.; Jeulin, D.: 3d multiscale vectorial simulations of random models. *Proc. ICS13, Beijing, 19-22 October 2011*.

Gibiansky, L.; Milton, G.: On the effective viscoelastic moduli of two-phase media. i. rigorous bounds on the complex bulk modulus. *Proceedings of the Royal Society of London A: Mathematical, Physical and Engineering Sciences*, 440, 1908, (1993), 163–188.

Hashin, Z.: Complex moduli of viscoelastic composites–i. general theory and application to particulate composites. *International Journal of Solids and Structures*, 6, 5, (1970), 539–552.

Jean, A.; Jeulin, D.; Forest, S.; Cantournet, S.; N'Guyen, F.: A multiscale microstructure model of carbon black distribution in rubber. *Journal of Microscopy*, 241, 3, (2011a), 243–260.

Jean, A.; Willot, F.; Cantournet, S.; Forest, S.; Jeulin, D.: Large scale computations of effective elastic properties of rubber with carbon black fillers. *International Journal for Multiscale Computational Engineering*, 9, 3, (2011b), 271–303.

Jeulin, D.: *Modèles morphologiques de structures aléatoires et de changement d'échelle*. Thèse d'état (1991).

Jeulin, D.: Multi scale random models of complex microstructures. In: *Materials Science Forum*, vol. 638, pages 81–86, Trans Tech Publ (2010).

Jeulin, D.: Morphology and effective properties of multi-scale random sets: A review. *Comptes Rendus Mécanique*, 340, 4, (2012), 219–229.

Jeulin, D.; Le Cöent, A.: Morphological modeling of random composites. *Proceedings of the CMDS8 58 Conference, Varna, Bulgaria*.

Jha, V.; Thomas, A.; Fukahori, Y.; Busfield, J.: Micro-structural finite element modelling of the stifness of filled elastomers: the effect of filler number,shape and position in the rubber matrix. *Proceedings of 5th European Conference on Constitutive Models for Rubber, ECCMR 2007, Paris, France*.

Kanit, T.; Forest, S.; Galliet, I.; Mounoury, V.; Jeulin, D.: Determination of the size of the representative volume element for random composites: statistical and numerical approach. *International Journal of Solids and Structures*, 40, 13, (2003), 3647–3679.

Laiarinandrasana, L.; Jean, A.; Jeulin, D.; Forest, S.: Modelling the effects of various contents of fillers on the relaxation rate of elastomers. *Materials & Design*, 33, (2012), 75–82.

Levenberg, K.: A method for the solution of certain problems in least squares. *Quarterly of Applied Mathematics*, 2, (1944), 164–168.

Matheron, G.: *Introduction aux ensembles aléatoires*. Ecole des Mines de Paris (1969).

Matheron, G.: *Random sets and integral geometry*. Wiley New York (1975).

Meyer, F.: Iterative image transformations for an automatic screening of cervical smears. *Journal of Histochemistry & Cytochemistry*, 27, 1, (1979), 128–135.

Michel, J.-C.; Moulinec, H.; Suquet, P.: A computational scheme for linear and non-linear composites with arbitrary phase contrast. *International Journal for Numerical Methods in Engineering*, 52, 1-2, (2001), 139–160.

Milton, G.; Berryman, J. G.: On the effective viscoelastic moduli of two–phase media. ii. rigorous bounds on the complex shear modulus in three dimensions. In: *Proceedings of the Royal Society of London A: Mathematical, Physical and Engineering Sciences*, vol. 453, pages 1849–1880 (1997).

Møller, J.: Random tessellations in $\mathbb{R}^d$. *Advances in Applied Probability*, pages 37–73.

Møller, J.: Random johnson-mehl tessellations. *Advances in applied probability*, pages 814–844.

Moreaud, M.; Jeulin, D.: Multi-scale simulation of random spheres aggregates: Application to nanocomposites. *Proceedings of the ECS 9 Conference, Zakopane, Poland*, pages 341–348.

Moulinec, H.; Suquet, P.: A fast numerical method for computing the linear and non linear mechanical properties of the composites. *Comptes rendus de l'Academie des sciences, Série II*, 318, 11, (1994), 1417–1423.

Naito, M.; K., M.; Azuma, K.; Tomita, Y.: 3d modeling and simulation of micro to macroscopic deformation behavior of filled rubber. *Proceedings of 5th European Conference on Constitutive Models for Rubber, ECCMR 2007, Paris, France*.

Nelder, J. A.; Mead, R.: A simplex method for function minimization. *Computer Journal*, 7, 4, (1965), 308–313.

Savary, L.; Jeulin, D.; Thorel, A.: Morphological analysis of carbon-polymer composite materials from thick sections. *Acta Stereologica (Slovenia)*, 18, 3, (1999), 297–303.

Schneider, R.; Weil, W.: *Stochastic and integral geometry*. Springer (2008).

Serra, J.: *Image analysis and mathematical morphology*. Academic Press, Inc. (1982).

Stoyan, D.; Kendall, W. S.; Mecke, J.: *Stochastic geometry and its applications*. Akademie-Verlag, Berlin (1995).

Vinogradov, V.; Milton, G.: An accelerated fft algorithm for thermoelastic and non-linear composites. *International Journal for Numerical Methods in Engineering*, 76, 11, (2008), 1678.

Willot, F.: Fourier-based schemes for computing the mechanical response of composites with accurate local fields. *Comptes rendus de l'Académie des Sciences: Mécanique*, 343, 3, (2015), 232–245.

Willot, F.; Abdallah, B.; Pellegrini, Y.-P.: Fourier-based schemes with modified green operator for computing the electrical response of heterogeneous media with accurate local fields. *International Journal for Numerical Methods in Engineering*, 98, 7, (2014), 518–533.

Willot, F.; Pellegrini, Y.-P.: Fast Fourier transform computations and build-up of plastic deformation in 2D, elastic-perfectly plastic, pixelwise-disordered porous media. In: *D. Jeulin, S. Forest (eds), "Continuum Models and Discrete Systems CMDS 11"*, pages 443–449, École des Mines, Paris (2008).

Zähle, M.: Random cell complexes and generalised sets. *The Annals of Probability*, pages 1742–1766.

Address: Bruno Figliuzzi, Dominique Jeulin, Matthieu Faessel, Franois Willot, PSL Research University 35, rue Saint Honor F-77305 Fontainebleau Cedex, France
email: bruno.figliuzzi@mines-paristech.fr, dominique.jeulin@mines-paristech.fr, matthieu.faessel@mines-paristech.fr,franois.willot@mines-paristech.fr

Address: Masataka Koishi, Naoya Kowatari, KOISHI Lab. R and D Center The Yokohama Rubber Co.,Ltd. 2-1 Oiwake, Hiratsuka Kanagawa 254-8601, Japan
email: masataka.koishi@y-yokohama.com, naoya.kowatari@y-yokohama.com